Research Paper

GEOSPHERE

GEOSPHERE, v. 20, no. 5

https://doi.org/10.1130/GES02702.1

9 figures; 1 supplemental file

CORRESPONDENCE: rilbhaskar@gmail.com

CITATION: Senapati, B., Kundu, B., Jin, S., and Santosh, M., 2024, Drought-induced seismicity modulation in the New Madrid Seismic Zone, central United States: Geosphere, v. 20, no. 5, p. 1347–1363, https://doi.org/10.1130/GES02702.1.

Science Editor: Andrea Hampel
Associate Editor: Craig H. Jones

Received 24 July 2023
Revision received 12 June 2024
Accepted 25 June 2024

Published online 26 August 2024

Drought-induced seismicity modulation in the New Madrid Seismic Zone, central United States

Batakrushna Senapati[1], Bhaskar Kundu[1], Shuanggen Jin[2,3], and M. Santosh[4,5,6]

[1]Department of Earth and Atmospheric Sciences, National Institute of Technology Rourkela (NITR), Rourkela 769008, India
[2]School of Surveying and Land Information Engineering, Henan Polytechnic University, Jiaozuo 454003, China
[3]Shanghai Astronomical Observatory, Chinese Academy of Sciences, Shanghai 200030, China
[4]School of Earth Sciences and Resources, China University of Geosciences, Beijing 100083, China
[5]Department of Earth Science, University of Adelaide, Adelaide, SA 5005, Australia
[6]Faculty of Science, Kochi University, Kochi 780-8520, Japan

ABSTRACT

The New Madrid Seismic Zone (NMSZ) in the central United States is a seismically active intraplate region composed of two fault segments: the Reelfoot and Cottonwood Grove fault segments. It has witnessed several major earthquakes, including a devastating 1811–1812 earthquake sequence of three ~M7 events. Nearly 200 years later, earthquakes still continue today in this complex seismic zone. This seismic zone is located in a domain with higher hydrological load than surrounding regions, which may play a crucial role in seismicity modulation. However, the hydrological unloading or loading-induced seismicity modulation and the underlying earthquake dynamics on this stable plate interior remain equivocal. Our study demonstrates that increased climate variability and drought-induced hydrological unloading can be potential drivers for the crustal stress change in the upper Mississippi embayment and seismicity modulation in the NMSZ. The seismicity rate associated with the Reelfoot fault segment shows ~60% increase during drought-induced prolonged drier periods, linked to La Niña cycles, than during the relatively wetter periods. However, such a feature is lacking for the seismicity associated with the Cottonwood Grove fault segment. We argue that the near-lithostatic pore pressure condition explicitly on the Reelfoot fault segment leads to an increase in the amplitude of the velocity perturbation, making this fault segment more susceptible to seismicity modulation on a multi-annual or annual time scale by the resonance destabilization process.

INTRODUCTION

Although faulting in general is driven by tectonic loading forces, there are also several other non-tectonic processes that can contribute to fault movements, such as hydrological loading, reservoir loading, and tidal loading, and are capable of influencing the seismicity in both regions with high strain rate (i.e., plate boundary regions) and those with low strain rate (i.e., stable plate interior) (Roeloffs, 1988; King et al., 1994; Stein, 1999; Camelbeeck et al., 2007; Bettinelli et al., 2008; Calais and Stein, 2009; Deng et al., 2010; Calais et al., 2016; Kundu et al., 2017; Panda et al., 2018; Craig et al., 2017, 2023). Among these, hydrological loading, which influences the terrestrial water storage on the Earth's surface by redistributing the hydrological cycle on a seasonal scale all around the globe, is the dominant non-tectonic process (Fu et al., 2012; Chanard et al., 2014). Furthermore, global meteorological events associated with prolonged drier and hotter conditions due to climate variability will also drive regional terrestrial water storage change. This causes hydrological load variations on the Earth's surface, which are also an important factor for influencing the spatiotemporal behavior of earthquake occurrences in some regions (Young et al., 2021). Annual surface load–induced strain variations have been linked to seasonal seismicity variations (Bollinger et al., 2007; Bettinelli et al., 2008; Craig et al., 2017; Johnson et al., 2017), although evidence for temporally variable and drought-induced inter-annual (or multi-annual) seismicity modulations in stable plate interiors and the associated earthquake physics remains equivocal.

In this study, we investigate the role of increased climate variability and prolonged drought-induced hydrological surface-load variation in crustal stress accumulation at the upper Mississippi embayment and the seismicity variation in the New Madrid Seismic Zone (NMSZ) in the central United States (Fig. 1A; Fig. S1 in the Supplemental Material[1]). The NMSZ is a seismically active intraplate region that has witnessed several major earthquakes (Craig and Calais, 2014). This seismic zone is located in a domain with higher hydrological load than surrounding regions, which may play a significant role in seismicity modulation (Fig. S1). However, the hydrological unloading or loading-induced seismicity modulation and the underlying fault dynamics on this stable plate interior are poorly understood.

Further, the soil moisture and climatic patterns over the Mississippi Basin are strongly affected by El Niño–Southern Oscillation (ENSO), a climatic

Bhaskar Kundu https://orcid.org/0000-0001-6171-884X

[1]Supplemental Material. Contains methodology, figures, and tables. Please visit https://doi.org/10.1130/GEOS.S.26308126 to access the supplemental material, and contact editing@geosociety.org with any questions.

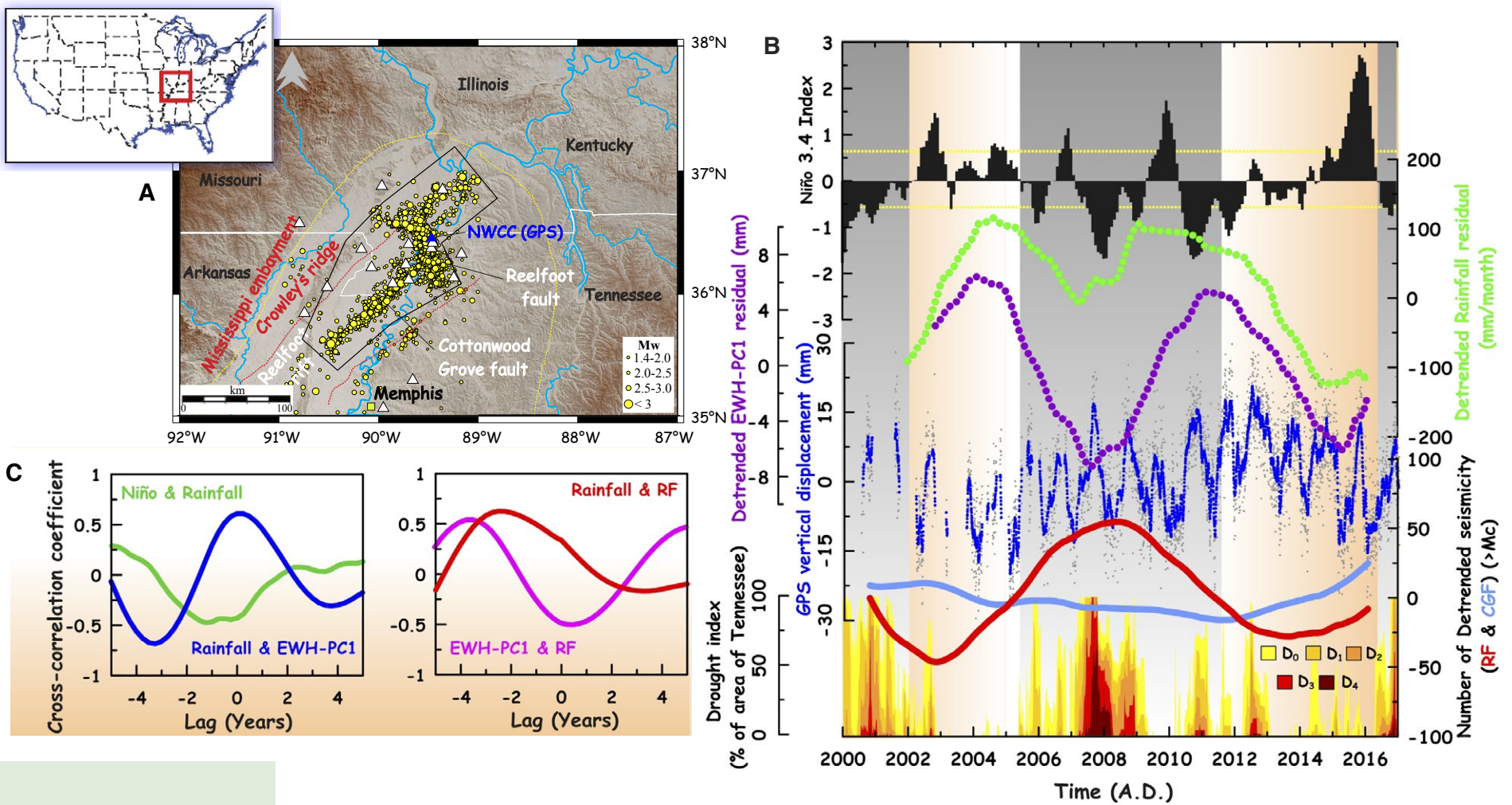

Figure 1. (A) Epicentral distribution of magnitude-wise declustered seismicity (magnitude completeness [Mc] = 1.4) (represented by yellow circles) for the period 2000–2016. New Madrid Seismic Zone is outlined by a black polygon. White triangles represent continuous GPS (cGPS) sites. NWCC is a cGPS site whose vertical displacement component shown in Figure 1B. (B) Time-series representation for Niño 3.4 index (Munoz and Dee, 2017), rainfall, equivalent water height (EWH), principal component (PC), cGPS vertical displacement, seismicity greater than the magnitude completeness (Mc = 1.4) associated with with Reelfoot fault (RF) and Cottonwood Grove fault (CGF), and drought index. Gray dots and blue line are the actual and running average of vertical displacement of NWCC site. Gray shading represents drought periods. Note D_0, D_1, D_2, D_3, and D_4 indicate abnormally dry, moderate drought, severe drought, extreme drought, and exceptional drought, respectively. (C) Lag correlation coefficient between rainfall, EWH, Niño 3.4 index, and seismicity of the RF. Note that there is a higher seismicity rate during the drought period, which is marked by gray shading in B.

phenomenon associated with sea-surface-temperature anomalies in the eastern equatorial Pacific (Gershunov and Barnett, 1998; Smith et al., 1998; Munoz and Dee, 2017). The warm and cold phases of ENSO are called El Niño and La Niña, respectively. During the El Niño phase, floods occur in the Mississippi Basin, e.g., the flooding events during 1927 and 2011 were preceded by the 1925–1926 and 2009–2010 El Niño phases, respectively (Munoz and Dee, 2017). In contrast, during 2007–2008 and 2010–2011, the La Niña phase caused drought conditions in the Mississippi Basin (Munoz and Dee, 2017). Therefore, the ENSO phenomena might have a control on the regional terrestrial water storage changes in the Mississippi Basin region and the central United States, influencing the earthquake occurrences in these regions. Moreover, from 2000 to 2016, seismic instrumentation and network distribution were comparatively uniform and stable in the NMSZ (Craig et al., 2017), and the La Niña phases of the ENSO event also caused drought conditions during this time (Munoz and Dee, 2017). Hence, the prolonged drought condition linked to the ENSO events in the NMSZ in the 21st century provides a unique window to explore drought-induced seismicity modulation in this region.

GENERAL TECTONICS OF THE NMSZ

The NMSZ in the central United States is the most seismically active intraplate region located east of the Rocky Mountains. The NMSZ has hosted several major earthquakes over the last several thousand years (Tuttle et al., 2005; Gold et al., 2019), including a devastating 1811–1812 earthquake sequence of three ~M7 events (Bakun and Hopper, 2004; Hough and Page, 2011; Boyd and Cramer, 2014). The NMSZ is located within the northeast-southwest–trending Reelfoot failed rift arm, which developed during the late Proterozoic and early Cambrian opening of the Iapetus Ocean (Ervin and McGinnis, 1975). Four prehistoric earthquakes since 11 ka have been reported based on paleoseismic trenching of sackungen along the Reelfoot failed rift arm (Gold et al., 2019). Smaller earthquakes continue today on the complex fault segments that ruptured during 1811–1812 (Tuttle et al., 2005; Calais et al., 2010; Bisrat et al., 2012), possibly representing a particularly enduring aftershock sequence of these events (Stein and Liu, 2009). Despite the subdued topography, lack of heat-flow anomaly (McKenna et al., 2007), and insignificant continuous GPS (cGPS)-derived deformation rates (~0.2 mm/yr) (Craig and Calais, 2014), the paleoseismic evidence and high seismicity rates nearly 200 years after the devastating earthquake sequence have been interpreted to indicate high earthquake hazard (Williams, 2009). On the other hand, Stein and Liu (2009) argued that if the current micro-seismicity represents a long-lasting aftershock sequence in a slowly deforming plate interior region, a lower seismic hazard may be indicated.

The distribution of micro-seismicity illuminates a complex network of faults and deformation styles within the NMSZ. Seismicity is associated mainly with two principal fault systems, i.e., the Reelfoot thrust fault (considered a step-over arm) and the right-lateral Cottonwood Grove fault (Calais et al., 2010) (Fig. 1A; Fig. S1, see footnote 1). The Reelfoot fault is the most seismically active structure compared to Cottonwood Grove fault and also produced several micro-seismic swarms and repeating earthquakes (Bisrat et al., 2012). Seismic instrumentation and network geometry have evolved since 1974, when instrumental monitoring was initiated in the region. Since 2000, the overall network coverage has remained relatively stable (Craig et al., 2017).

DATA AND METHODS

Data Sets

In order to characterize the seismicity modulation in the NMSZ region induced by the hydrological load and establish the relation between climate variability and seismicity, we have analyzed multiple data sets, including the seismicity data surrounding the NMSZ region, weekly drought index, Niño 3.4 index, equivalent water height (EWH), cGPS data, and monthly rainfall data. The seismicity data surrounding the NMSZ region for the period of 2000–2016 are maintained by the Center for Earthquake Research and Information at the University of Memphis, Tennessee, USA (https://www.memphis.edu/ceri/seismic/nm_cat_help.php). The monthly Niño 3.4 index data are controlled by the National Oceanic and Atmospheric Administration (https://www.ncei.noaa.gov/access/monitoring/enso/). The weekly drought index data over the NMSZ region are controlled and maintained by the U.S. Drought Monitor (https://droughtmonitor.unl.edu/). EWH variation over the NMSZ is obtained from the Gravity Recovery and Climate Experiment (GRACE) satellite data for the period 2002–2016 (https://grgs.obs-mip.fr/). The cGPS data used in the present study are archived at the Nevada Geodetic Laboratory (http://geodesy.unr.edu). The monthly rainfall data from the Tropical Rainfall Measuring Mission (http://www.esrl.noaa.gov/psd/) is archived at the Global Precipitation Climatological Centre (http://www.esrl.noaa.gov/psd/).

Magnitude Completeness (Mc) and Declustering Approach

We have analyzed the Gutenberg-Richter relation [$\log N(M \geq Mc) = a' - b' \times Mc$] of the seismicity associated with the NMSZ, Reelfoot fault, and Cottonwood Grove fault by employing the maximum likelihood approach (Aki, 1965) to estimate the magnitude completeness (Mc). This Mc value represents the minimum magnitude above which all seismicity are statistically reliable for further analysis. a' and b' are essential seismic parameters in assessing probabilistic seismic hazard. M is the magnitude of the earthquakes and N is the number of events. The magnitude completeness of the seismicity catalogs is estimated to be 1.4 for the seismicity associated with the NMSZ, Reelfoot fault, and Cottonwood Grove fault (Fig. S2, see footnote 1). Following this, a declustered earthquake catalog is also generated based on the nearest-neighbor analysis of seismicity following the Zaliapin and Ben-Zion (2020) approach (for details, see the Supplemental Material).

Periodicity Analysis

In order to estimate the periodicity of the seismicity associated with the NMSZ, Reelfoot fault, and Cottonwood Grove fault, we have computed the spectra of Schuster probability (*p*)-values by considering the methodology proposed by Ader and Avouac (2013). For the computation of probability, the timing of events (t_k) in a catalog varies according to a sine-wave function of period *T*, which is associated with the phase (θ_k) represented as $\theta_k = 2\pi\frac{t_k}{T}$. Further, the probability that arises due to the difference in event-time distribution from a uniform seismicity rate can be expressed as (Ader and Avouac, 2013):

$$p = e^{-D^2/N}, \tag{1}$$

where *p* is the Schuster probability value, *N* is the number of events in the seismicity catalog, and *D* is the time span between the start and end point of the seismicity catalog (Ader and Avouac, 2013). Further, we have also analyzed the periodicity of the seismicity associated with the Reelfoot fault and Cottonwood Grove fault using the power spectra density analysis by generating continuous seismicity time series by converting the entire period of the earthquake time series into the number of events per hour (for details, see the Supplemental Material).

Principal Component Analysis

Principal component (PC) analysis involves collection of the covariance information contained in a time series over a sliding *M*-point window (Broomhead and King, 1986; Plaut and Vautard, 1994; Ghil et al., 2002; Groth and Ghil, 2015). It is a generalization of this approach to systems of partial differential equations and the study of spatiotemporal structures that characterize the behavior of solutions on their attractor (Constantin et al., 1989; Temam, 1997). First, it creates a matrix that contains *M* time–delayed copies of the original time series. After that, it computes the covariance matrices between all pairs of time series, which are used as blocks of a grand covariance matrix that contains both spatial and temporal correlations. Here, we have used multichannel singular spectrum analysis in order to capture the multi-annual signal included in the EWH time series, considering *M*-point window as 30 days (for details, see the Supplemental Material)

Quantification of Normal and Shear Stress from EWH

The hydrological stress variation can be expressed in terms of the EWH of the region (see the Supplemental Material for EWH estimation from GRACE data). In that case, the vertical stress perturbation caused by the hydrological load can be expressed as:

$$\sigma_{zz} = \rho_w g h, \tag{2}$$

where σ_{zz} is the vertical stress change, ρ_w is the density of the water, g is the acceleration due to gravity, and *h* is the water column thickness derived from peak-to-peak EWH from GRACE observation (in millimeters). Here, we assume that Equation 2 also relates to perturbation to the vertical principal stress at the depth of shallow earthquakes. We have also estimated the horizontal stresses, σ_{xx} and σ_{yy}, from the peak-to-peak EWH assuming uniaxial strain (Turcotte and Schubert, 2002):

$$\sigma_{xx} = \sigma_{yy} = \frac{\vartheta}{1-\vartheta}\sigma_{zz}, \tag{3}$$

where ϑ is Poisson's ratio (0.25).

The hydrological load perturbations to the normal (σ_n) and shear (τ_s) stress acting on a fault are expressed as (Jaeger and Cook, 1979):

$$\left.\begin{aligned}\sigma_n &= \sigma_{zz}\left(\cos^2\delta + \frac{\vartheta}{1-\vartheta}\sin^2\delta\right)\\ \tau_s &= \sigma_{zz}\frac{2\vartheta-1}{1-\vartheta}\sin\delta\cos\delta\sin\lambda\end{aligned}\right\}, \tag{4}$$

where δ is the dip of the fault and λ is the rake of fault. In the present computation, we have considered strike 47°, dip 85°, and rake +180° for Cottonwood Grove fault and strike 173°, dip 32°, and rake +90° for Reelfoot fault. The estimated normal and shear stress for the Cottonwood Grove fault and Reelfoot fault are represented in Figure S3.

Estimation of Strain and Stress from cGPS Seasonal Displacements

The cGPS-derived displacement was used for the estimation of the strain field in the NMSZ region. In the present study, we have used the SSPX computer program (an application to compute strain from displacement or velocity data in two and three dimensions; Cardozo and Allmendinger, 2009) to estimate the strain in the NMSZ region. SSPX works using both the nearest-neighbor and distance-weighted approach on a regularly spaced grid and calculates the displacement gradient at each node in the grid. The distance-weighted approach produces a smoother strain than the nearest-neighbor approach and is particularly effective for visualizing regional strain patterns. In the distance-weighted approach, all the cGPS sites (marked in Fig. 1A; Table S1, see footnote 1) are used in the calculation, but data from each station are weighted by their distance from the grid node by a specific constant, α, that specifies how the effect of a station decays with distance from the node (Shen et al., 1996). Each datum is weighted by a factor (*W*) expressed as:

$$W = \exp\left(\frac{-d^2}{2\alpha^2}\right), \tag{5}$$

where *d* is the distance between the node and a station. Stations within a 1α distance contribute more than 67% to the least square solution, whereas those

at greater than 3α distance contribute less than 1%. The weighting factor, *W*, is a diagonal matrix and included in the inversion as (Menke, 1984):

$$m = \left[G^T W G\right]^{-1} G^T u, \tag{6}$$

where *G* is the design matrix, *T* is the time period, *u* is the column vector of horizontal displacement, and *m* is the column vector of unknown displacement gradients and translations. We have estimated the extension, shortening, maximum shear strain, and dilation at the cGPS sites and in each significant cell for the NMSZ. We have taken a grid spacing of 10 km and used a distance-weighted algorithm with α = 20 km. The value of α is chosen so that it yields maximum variation in the parameter of interest with the minimum number of insignificant nodes, where the absolute value of the magnitude is less than one uncertainty.

Coulomb Failure Stress Change from EWH

The effect of seasonal unloading on the Earth's crust and fault system can be quantified by the Coulomb failure stress change (ΔCFS). For this, it is necessary to estimate the stress caused by the vertical line load (N_0 in N/m) at a point (*p*) within a homogenous elastic half-space at a given depth. The different stress components (σ_{xx}, σ_{zz}, and σ_{xz}) are expressed as a function of the geometrical position of the load (Jaeger et al., 2007; Boussinesq, 1885), given as:

$$\left.\begin{aligned}
\sigma_{xx} &= \frac{N_0}{\pi a}\left[(\theta_1-\theta_2)+\sin(\theta_1-\theta_2)\cos(\theta_1+\theta_2)\right]\\
\sigma_{zz} &= \frac{N_0}{\pi a}\left[(\theta_1-\theta_2)-\sin(\theta_1-\theta_2)\cos(\theta_1+\theta_2)\right]\\
\sigma_{xz} &= \frac{N_0}{\pi a}\left[\sin(\theta_1-\theta_2)\sin(\theta_1+\theta_2)\right]
\end{aligned}\right\}, \tag{7}$$

where θ_1 and θ_2 are the angles measured clockwise from the positive x direction from two edges of the line load, *a* is the width of the load, and z is positive downward. The normal (σ_n) and shear stress (τ) are resolved on a fault plane that dips at an angle of δ with a direction of strike normal to the xz-plane, and are represented as:

$$\left.\begin{aligned}
\sigma_n &= \sigma_{xx}\sin^2(\delta)+2\sigma_{xz}\sin(\delta)\cos(\delta)+\sigma_{zz}\cos^2(\delta)\\
\tau &= (\sigma_{zz}-\sigma_{xx})\sin(\delta)\cos(\delta)+\sigma_{xz}(\sin^2(\delta)-\cos^2(\delta))
\end{aligned}\right\}. \tag{8}$$

The ΔCFS is given as:

$$\Delta\mathrm{CFS} = |\tau| + \mu(\sigma_n), \tag{9}$$

where μ is the fault friction coefficient.

Rainfall-Induced Poroelastic Model

We computed the pore-fluid pressure changes at depth in response to surface rainfall under assumption of one-dimensional half-space with spatially uniform but temporarily varying rainfall in the region. In the coupled hydro-mechanical process of fluid pressure, relaxation can be characterized by dynamics of a fluid-saturated poroelastic solid medium (Biot, 1962). Using a finite difference approximation scheme to solve the transient and vertical groundwater flow, we have quantified the subsurface pore pressure perturbations as a function of rainfall, which represents a classical diffusion problem under mathematical approximations such as (Barton, 1989; Rudnicki, 1986):

$$\frac{\delta p}{\delta t} = \left[\frac{kB}{\gamma\phi}\right]\left[\frac{\delta^2 p}{\delta z^2}\right], \tag{10}$$

where the change in pore pressure (*p*) in time *t* at depth *z* is a function of the permeability (*k*), bulk modulus (*B*), and porosity (ϕ) of the constituent and the viscosity (γ) of the saturating fluid. The first term $kB/\gamma\phi$ of the equation is the coefficient of hydraulic diffusion. The zero pressure change is given at the base of the domain to have a zero-flux boundary, *Z*, of the assumed domain at 20 km below the surface, $(\partial p/\partial z)_{z=Z} = 0$. The depth is enough to allow us to neglect any boundary effect (Farquharson and Amelung, 2020). Surface pressure is expressed as $p(z = 0, t) = \varrho_w g h(t)$, where *h* is rainfall recorded height at time *t*, ϱ_w is the density of percolating water, and g is gravitational acceleration. Model sensitivity to rainfall input shows relative timing and pressure evolution magnitude have negligible variation (Farquharson and Amelung, 2020). Further, we acknowledge that the hydro-magmatic and tectonic framework of the NMSZ region is complex; however, in the absence of accurate estimates of hydrological parameters beneath the NMSZ region, we have adopted representative hydrogeological model parameters from Farquharson and Amelung (2020) (Table S2).

Hydrological Load–Induced Fault Resonance Model

It has been proposed that a creeping fault can destabilize under the influence of external periodic stress perturbations (Perfettini et al., 2001; Perfettini and Schmittbuhl, 2001; Senapati et al., 2022, 2023). It has also been suggested that the slip response due to an external stress oscillation can be amplified within a narrow band of resonant periods; in that situation, the external periodic stress (i.e., hydrological load in the present case) can cause slip perturbation (V_1) at period *T*, which can be expressed by:

$$\left.\begin{aligned}
V_1 &= qV_{rfm}\frac{q\left[\sigma_1(\mu_{ss}-\alpha)-\tilde{\tau}\right]-i(\sigma_1-\tilde{\tau})}{\left(kd_c-a\sigma_n q^2\right)+iqd_c(K-K_c)}\\
q &= \frac{2\pi d_c}{TV_{rfm}}\\
K_c &= \frac{\sigma_n(b-a)}{d_c}
\end{aligned}\right\}, \tag{11}$$

where V_1 is the amplitude of slip perturbation, q is the dimensionless pulsation, V_{rfm} is fault motion velocity, μ_{ss} is the steady-state frictional coefficient, d_c is the critical slip distance, α is the frictional response to change in normal stress, K is the fault elastic stiffness, a and b are frictional parameter, σ_1 and $\tilde{\tau}$ are the external normal and shear stress perturbation, respectively. Slip resonance occurs at critical stiffness (i.e., at $K = K_c$), which occurs at the critical time period (T_c):

$$T_c = \frac{2\pi d_c}{TV_{rfm}}\sqrt{\frac{a}{(b-a)}}. \quad (12)$$

The amplitude of slip perturbation approaches its maximum value at narrow ranges of critical time periods (T_c) and for small periods when $K/K_c = 1.002$. Further, we have also estimated the frictional parameters ($\varepsilon = \frac{b}{a} - 1$, $A = a\sigma_n$, d_c, T_c/T, h_*/h) to test the possibility of resonance amplification in the NMSZ region. ε is the ration of friction parameter a and b, A is the normalized normal stress, and h_* is the critical length of the fault slip patch. Each of these frictional parameters is estimated by minimizing the cost function C, which is expressed as

$$C = \sqrt{\frac{\left(1-\frac{T}{T_c}\right)^2 + \left(1-\frac{h}{h_*}\right)^2}{2}}. \quad (13)$$

The model estimated parameters (i.e., T_c/T; h_*/h; and ε and C) for the resonance process are shown in Figure S4 and Tables S3 and S4.

RESULTS

Hydrological Unloading–Induced Seismicity Modulation in the NMSZ

To understand climate-induced hydrological load variations and seismicity modulation, we have explored the connections among the indicators for global inter-annual climate variability, ENSO, anomalous precipitation in mid-tropical regions, signatures in the Earth's gravity fields through a change in continental water storage (i.e., GRACE-derived EWH), cGPS displacements, regional drought index, and seismicity associated with two principal structures in the NMSZ (Cottonwood Grove fault and Reelfoot fault) (Fig. 1B; Fig. S5 [see footnote 1]). La Niña conditions are usually associated with drier and hotter conditions and exacerbation of droughts in California, USA, and in the central, southwestern, and to some extent, southeastern United States (Munoz and Dee, 2017). Meanwhile, El Niño conditions cause a positive precipitation anomaly over the Mississippi embayment. This causes a gradual build-up of soil moisture in the Mississippi embayment and reduces the optimum capacity of the basin's infiltration, eventually elevating the risk of a major flood events (Munoz and Dee, 2017). Within our record, there are two consecutive periods of strong La Niña conditions (i.e., 2007–2008 and 2010–2011) that caused drought conditions over the Mississippi Basin. It is interesting to observe that the drought-induced drier periods exhibit a significantly higher frequency of seismicity linked with the Reelfoot fault segment in the NMSZ than relatively wetter periods. We also notice that the variation of the seismicity rate associated with the Reelfoot fault segment is correlated with the regional trend of continental water storage and precipitation. In contrast, the seismicity associated with the Cottonwood Grove fault segment does not exhibit such correlation. Moreover, we have computed the Schuster p-values for the declustered earthquake catalogs associated with the Reelfoot fault segment and observed that the Reelfoot fault segment exhibits statistically significant multi-annual periodicity (Fig. 2). Meanwhile, the Cottonwood Grove fault segment does not exhibit such multi-annual periodicity (Fig. 2). We have also found that the seismicity rate associated with the Reelfoot fault segment increases ~60% during dry periods relative to wet periods. The seismicity rate has a negative correlation with GRACE-derived continental water storage (i.e., specifically EWH-PC1) on the inter-annual time scale with cross-correlation coefficients of –0.55 (without any time lag or lead). Also, the regional precipitation is correlated with GRACE-derived continental water storage (i.e., specifically EWH-PC1) on the inter-annual time scale with coefficients of +0.65 (Fig. 1C).

Apart from the multi-annual periodicity, we have observed that the seismicity associated with the Reelfoot fault segment also exhibits relatively weak annual periodicity (Figs. 2 and 3) and the seismicity rate increases during the dry season (i.e., during low EWH) (Fig. 3). Moreover, we have also analyzed the cross-correlation between the seismicity, rainfall, and EWH and observed that seismicity rate is anti-correlated with GRACE-derived continental water storage on the annual scale with coefficients of –0.65 (with time lag of ~1 month). Similarly, the regional precipitation is correlated with GRACE-derived continental water storage with coefficients of +0.70 without showing any time lag or lead, whereas the vertical component of the cGPS data shows anti-correlation with GRACE-derived continental water storage with coefficients of +0.98 (Fig. 3). The lag between seismicity and rainfall suggests that the variation in seismicity rate is influenced by both (1) elastic stress change acting on the fault systems induced by hydrological load variation and (2) pore-fluid pressure variations. Based on the evidence gathered in our study, we suggest that drought-induced hydrological water loss over the Mississippi embayment and the seasonal unloading cycles induced crustal stress in the NMSZ on the order of a few kilopascals, which is capable of modulating the seismicity rate explicitly on the Reelfoot fault segment in this active but low-strain region (Figs. 1C and 3).

Surface Unloading–Induced Deformation and Stress Change

To quantify the geodetic horizontal strain patterns and the associated stress changes in the NMSZ region for the period 2000–2016, we have considered all the available cGPS stations (~20 sites) covering the NMSZ region (marked in Fig. 1A; Table S1). At first, we calculated the seasonal displacements during the hydrological unloading (May–September) and loading (October–April) period for 20 cGPS sites from monthly stacked cGPS time series (as shown in Fig. S6). Following this, the strain fields (i.e., extension, shortening, maximum shear strain, and dilation) are estimated from the derived seasonal

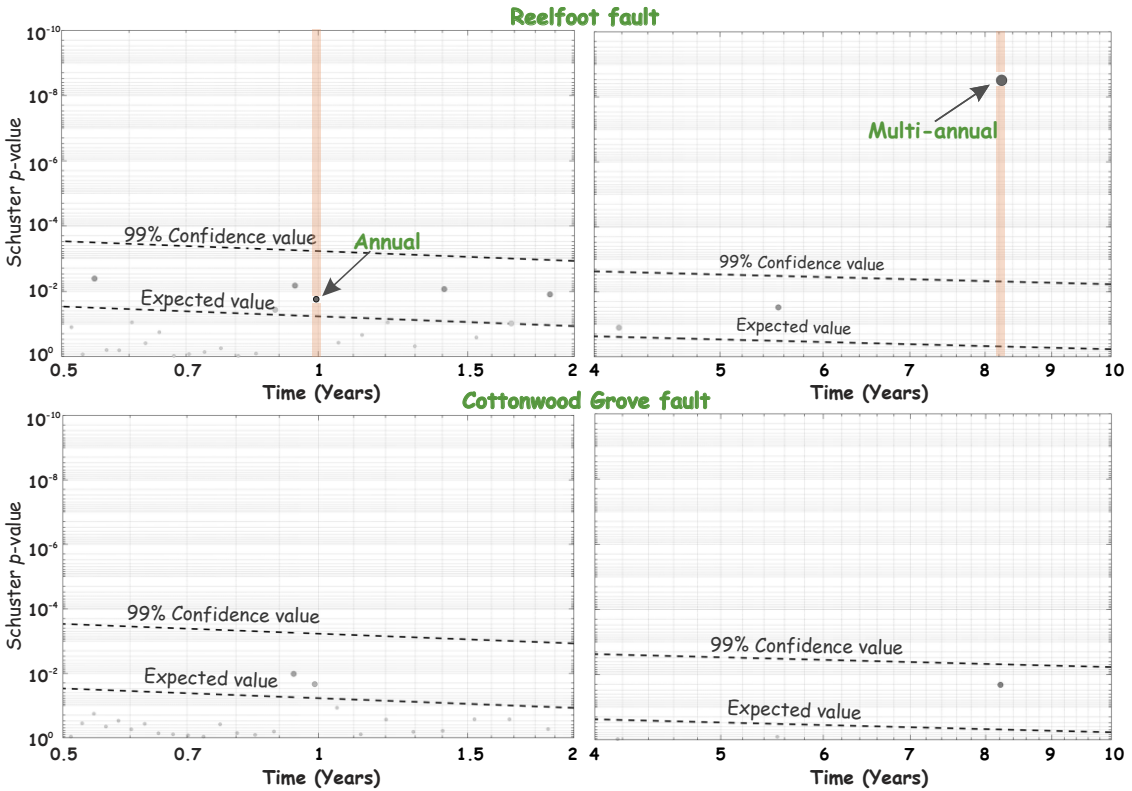

Figure 2. Schuster spectra for declustered seismicity (magnitude completeness = 1.4) for the Reelfoot fault and the Cottonwood Grove fault from 2000 to 2016. Orange stripe represents annual and multi-annual periodicity, respectively. Note that the Reelfoot fault exhibits a weak annual and significant multi-annual periodicity, whereas such periodicity is lacking in the case of the Cottonwood Grove fault.

displacement during the unloading period by using the SSPX application (Cardozo and Allmendinger, 2009; for details, see the Supplemental Material and Data and Methods section). Figure 4A represents the horizontal principal strain and dilatational strain derived from the geodetic seasonal displacements in the NMSZ. We observed that the compressional principal axes of horizontal strain in the Reelfoot fault region align in approximately NE-SW directions, whereas in the Cottonwood Grove fault region, they align in approximately NW-SE directions (Figs. 4A and 4B). The magnitudes of the seasonal dilatational strain anomalies are ~2×10^{-8} to ~3×10^{-8} in the NMSZ region. Further, we estimated the ΔCFS adopting the methodology proposed by Jaeger and Cook (1979) and resolved it on both the Reelfoot and Cottonwood Grove fault systems (Figs. 4C and 4D) (for details, see the Supplemental Material). We found that seasonal variations in horizontal strain related to drought produce a ΔCFS of ~0.2–0.4 kPa on the Reelfoot and Cottonwood Grove faults (Figs. 4C and 4D). We have also calculated the total horizontal change over the inter-annual time period of the drought (~2005–2012) from detrended cGPS time series (i.e., after removing long-term plate motion), estimated strain fields (i.e., extension, shortening, maximum shear strain, and dilation), and ΔCFS from the interannual horizontal displacement (Figs. S7 and S8). Here, we noticed that the magnitudes of the dilatational strain anomalies and ΔCFS during the interannual unloading period are less than the seasonal strain and ΔCFS (Figs. S7 and S8). The estimated ΔCFS is higher than the previously estimated critical threshold stress values of various exogenous forcings (Thomas et al., 2009; Hainzl et al., 2006; Kundu et al., 2015; Peng et al., 2009; Gomberg, 2010). However, Ziv and Rubin (2000) have argued for the threshold value of external stress perturbation for the earthquake-triggering process and suggested that no lower threshold exists for earthquake triggering in central California. Further, the ΔCFS on the Reelfoot and Cottonwood Grove faults are slightly lower than the ΔCFS in the Ridgecrest area in California (Kim et al., 2021). From this, we suggest that although the ΔCFS due to seasonal variations in horizontal strain may be capable of modulating the seismicity in both the Reelfoot and Cottonwood Grove fault systems, it is unable to explain why the Reelfoot fault shows seismicity modulation and the Cottonwood Grove fault does not.

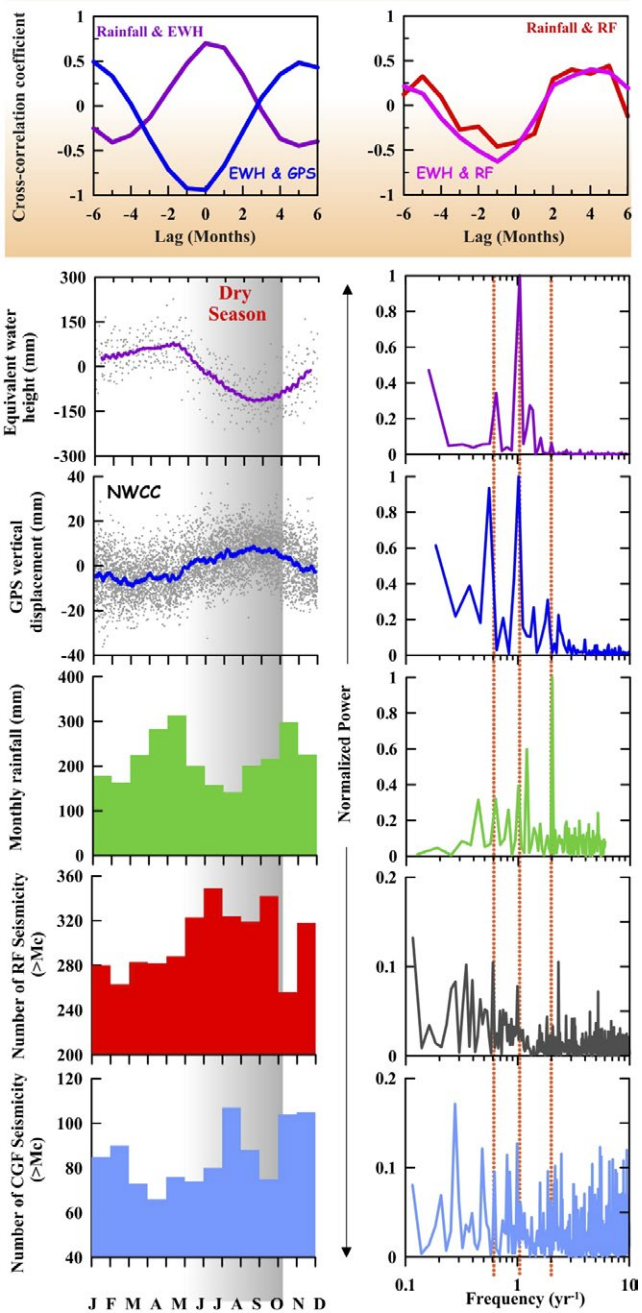

Figure 3. (Top panel) Lag correlation coefficient between rainfall, equivalent water height (EWH), continuous GPS (cGPS) vertical displacement, and seismicity of Reelfoot fault (RF). (Bottom panel, left) Monthly stacked peak-to-peak hydrological load variation (EWH), vertical cGPS displacement component of NWCC site marked in Figure 1A, monthly histogram of rainfall, and monthly histogram of declustered seismicity (magnitude completeness magnitude completeness [Mc] = 1.4) for the RF and Cottonwood Grove fault (CGF) region. Gray dots and blue line are the actual and running average of vertical displacement of NWCC site and EWH. (Bottom panel, right) Power spectrum analysis of EWH, cGPS vertical displacement of NWCC site, rainfall, and declustered seismicity (Mc = 1.4) for the RF and CGF. Orange dotted lines represent, from left to right, multi-annual, annual, and semi-annual periodicity.

Further, we have also estimated the variation in seasonal hydrological mass distribution over the NMSZ region by considering satellite data from GRACE from 2002 to 2016 (Fig. S9). We observed that the amplitude of hydrological load variation over the Reelfoot and Cottonwood Grove faults is overall similar (Fig. S9). In addition, we have also tried to model the surface deformation caused by the seasonal hydrological load variation at individual cGPS site coordinates. We notice that the GRACE-predicted displacements show a good match for the observed vertical displacements (Figs. S10). This suggested that the seasonal predictions appropriately predict both the amplitude and phase of the load-induced vertical surface displacement. But, in the case of horizontal components, there is a mismatch between the hydrological model–predicted displacement and the observed data (Figs. S11 and S12). This suggests that the horizontal displacement is influenced by other processes, such as poroelastic responses or thermoelastic changes, that probably were superimposed on the hydrologic response (Kraner et al., 2018; Kim et al., 2021). This prompted us to further explore the full stress response induced by the vertical load and the possible role of poroelastic deformation over the NMSZ region, which we discuss in the subsequent results sections.

Hydrological Unloading–Induced ΔCFS

We have estimated the ΔCFS for both the Reelfoot and Cottonwood Grove fault systems to quantify the hydrological unloading–induced ΔCFS in the NMSZ surrounding region (for details, see the Coulomb Failure Stress Change from EWH section). We have considered the length and the width of the Reelfoot fault to be ~115 km and 50 km, respectively, and the change in amplitude of EWH to be ~210 mm (Fig. S9), which gives an overall load distribution over the Reelfoot fault system of ~10.29×10^7 N/m. Then, we calculated the ΔCFS on a vertical section along a horizontal profile (i.e., along the strike of the fault) considering friction coefficient (μ) values of 0.2, 0.4, and 0.6, respectively (Fig. 5). For this analysis, we found that the ΔCFS for the Reelfoot fault is ~0.7–1.4 kPa at a depth of 6–8 km (i.e., hypocentral region of the earthquakes). Similarly, we have also calculated the ΔCFS for the Cottonwood Grove fault system, considering the length and width of the fault to be ~120 km and 30 km,

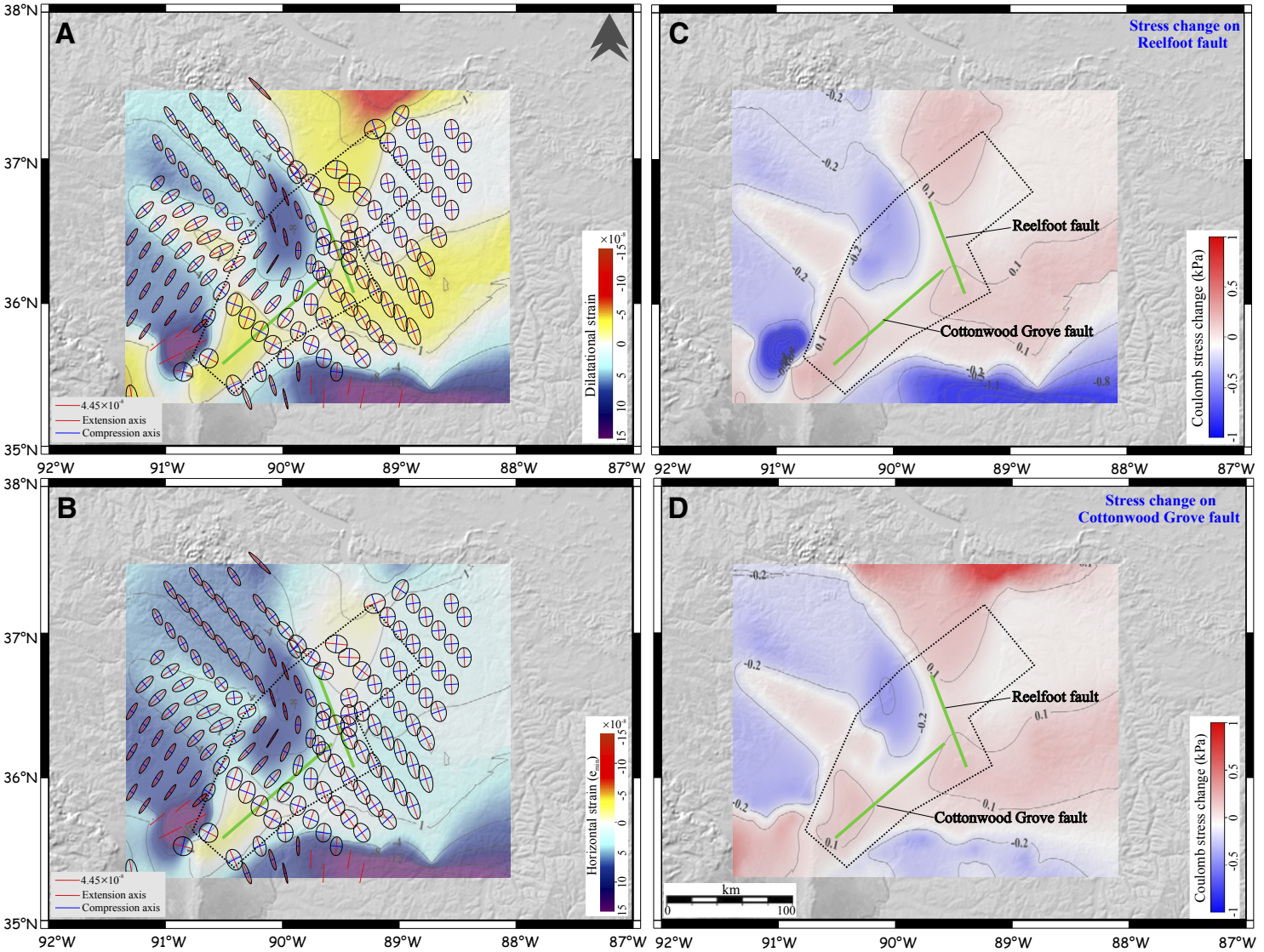

Figure 4. (A, B) Seasonal horizontal strain calculated from continuous GPS (cGPS) seasonal displacements between 2000 and 2016 (cGPS sites are marked in Fig. 1A). Principal axes of the nontectonic strain are shown by blue (compressional) and red (extensional) lines. Red line segment shown in the inset box represents scale of the horizontal strain. Background color plot is dilatational strain (A) and horizontal strain (B). Reelfoot and Cottonwood Grove faults are marked by green lines. (C, D) Coulomb failure stress changes (ΔCFS) calculated from seasonal horizontal strain, resolved on the Reelfoot fault (C) and Cottonwood Grove fault (D).

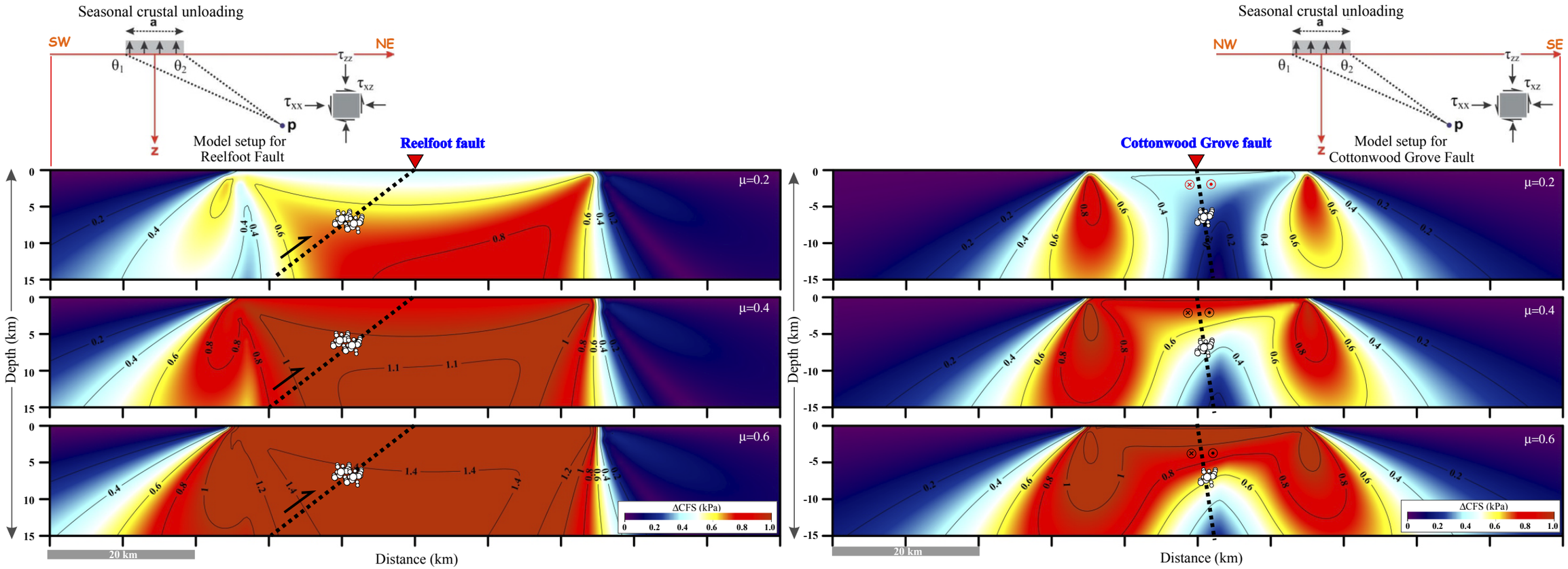

Figure 5. Coulomb failure stress change (ΔCFS) due to seasonal crustal unloading for Reelfoot fault (left panel) and Cottonwood Grove fault (right panel). Change in ΔCFS due to seasonal crustal unloading is plotted on a vertical section along a horizontal profile, considering friction coefficient (μ) values of 0.2, 0.4, and 0.6. ΔCFS is resolved on the subsurface fault dipping at 32° for Reelfoot fault and 85° for Cottonwood Grove fault. Model setup for Reelfoot fault and Cottonwood Grove fault is represented in the top left and right corners, respectively. Line load acting on the elastic half-space is distributed over width *a*. θ_1 and θ_2 measure the angle downward from the positive *x*-axis to any point *p* at depth. τ_{xx}, τ_{zz}, and τ_{xz} are different stress components. Note that ΔCFS is ~0.7–1.4 kPa for Reelfoot fault and 0.3–0.5 kPa for Cottonwood Grove fault at depth of 6–8 km, where maximum seismicity occurred in this region (white circles).

respectively, and similar amplitude of EWH, which gives a load distribution of ~6.7 × 10^7 N/m. We found that the ΔCFS for the Cottonwood Grove fault is ~0.3–0.5 kPa at a depth of 6–8 km (i.e., hypocentral region of the earthquakes) (Fig. 5). Further, it is observed that the critical threshold for stress perturbation value is ~0.15–0.3 kPa for tides (Thomas et al., 2009); less than 2 kPa for rainfall-induced earthquakes (Hainzl et al., 2006); 0.05–0.15 kPa/yr for groundwater unloading–induced triggering of 2015 Gorkha earthquake in Nepal (Kundu et al., 2015); 0.1–10 kPa for seismic waves (Peng et al., 2009; Gomberg, 2010); and 0.1–1 kPa for hydrological load–induced non-volcanic tremor along the Cascadia subduction zone, offshore western North America (Pollitz et al., 2013). Here, we also notice that the estimated ΔCFS in the Reelfoot and Cottonwood Grove faults is higher than the previously estimated critical threshold stress values of various exogenous forcings (Thomas et al., 2009; Hainzl et al., 2006; Kundu et al., 2015; Peng et al., 2009; Gomberg, 2010). Hence, we suggest that the ΔCFS due to seasonal unloading might be capable of modulating the seismicity in both Reelfoot and Cottonwood Grove fault systems, but it might not explain why the Reelfoot fault has more potential for hydrologically induced seismicity modulation than the Cottonwood Grove fault.

Rainfall-Induced Poroelastic Effects in the NMSZ

We computed pore-fluid pressure changes at depth in response to surface rainfall under assumption of one-dimensional half-space with spatially uniform but temporarily varying rainfall in the region, following the Farquharson and Amelung (2020) approach (for details, see the Rainfall-Induced Poroelastic Model section). The pore pressure change induced from rainfall is estimated with varying hydraulic diffusivity, permeability, and porosity with varying depth and considering other parameters, such as fluid (water) viscosity and bulk modulus constant (Table S2). From this analysis, we have observed that there is an insignificant increase in pore pressure build-up of ~10–20 Pa at the depth range of 6–10 km (Fig. 6). The sensitivity of the hydrological model parameters considered in the present study is presented in Figures 6A and 6B, which clearly demonstrate this pattern holds for a wide range of diffusivity and pore-pressure change as a function of depth. The variation of pore pressure change induced by rainfall as a function of depth with time is represented in Figures 6D and 6E. We have also calculated the variation of pore pressure change at depths of 6 km, 8 km, and 10 km and noticed that with increasing depth the pore pressure decreases (Fig. 6F). Further, we present linear correlation between pore pressure change at depths of 6 km, 8 km, and 10 km with seismicity associated with the Reelfoot and Cottonwood Grove fault systems. We observed that both Reelfoot fault and Cottonwood Grove fault show similar weak correlation (with correlation coefficient of 0.52) with pore pressure change (Figs. 6G and 6H). Therefore, we suggest that such rainfall-induced pore pressure change may not clearly explain the seismicity modulation process explicitly associated with the Reelfoot fault segment.

Hydrological Unloading–Induced Fault Resonance Model

Notably, both fault segments (Reelfoot and Cottonwood Grove faults) in the NMSZ belong to the same hydrological system, but the Reelfoot fault exhibits both annual and multi-annual periodicity, whereas the Cottonwood Grove fault does not exhibit any periodicity (Fig. 2). To address this ambiguity, we computed hydrological water loss–induced (i.e., regional drought cycle and seasonal cycle) external stress perturbation on the Reelfoot fault segment on the multi-annual and annual time scales by invoking the fault resonance process (Fig. 7). Figure 7 depicts the amplitude of velocity perturbation for varying pore-fluid pressure conditions as a function of stiffness (K), period (T), and stress change due to hydrological load variations (i.e., both for multi-annual and annual time scales). In this computation, we assumed a critical slip distance (d_c) of 10^{-6} m, critical period (T_c) of 8 yr for multi-annual and 1 yr for seasonal stress perturbation, steady-state frictional co-efficient (μ_{ss}) of 0.3, dimensionless frictional parameter ($b - a$) of 10^{-4}, and geodetically constrained deformation rates (V_{rfm}) of 0.2 mm/yr. These specific assumptions are compatible with laboratory estimates of rate-and-state-dependent frictional parameters (Perfettini et al., 2001; Perfettini and Schmittbuhl, 2001; Lowry, 2006; Panda et al., 2018; Senapati et al., 2022) and seismo-tectonic conditions of this stable plate-interior region (Craig and Calais, 2014). We suggest that the slip perturbation amplifies significantly within a very close range of period T_c, when the stiffness (K) is close to the critical stiffness (K_c) (Fig. 8A), and the amplitude of slip perturbation approaches its maximum value for $K/K_c = 1.002$ and is several times higher for low effective normal stress conditions (or high fluid pressure) (Fig. 8B). In other words, lowering of effective normal stress leads to an increase in the amplitude of the velocity perturbation both for multi-annual and annual time scales (Figs. 8A and 8B) and indicates near-lithostatic pore pressure conditions in the Reelfoot fault segment. Further, we also estimated the effective normal stress by adopting the methodology proposed by Senapati et al. (2023), and the results show that the effective normal stress of this region is ~11.4–0.0114 MPa, which also indicates the presence of high pore pressure conditions in the Reelfoot fault segment (Fig. S4; Tables S3 and S4). Hence, we suggest that the presence of high pore pressure conditions in the Reelfoot fault segment possibly places this fault segment in the conditional stable frictional regime, which is sensitive to periodic external stress perturbation induced by seasonal hydrological unloading and modulated seismicity on a multi-annual or annual time scale by the resonance process.

DISCUSSION

Several micro-seismic swarms and repeating earthquake sequences have been reported specifically on the Reelfoot fault segment, indicating fluid involvement and weak, aseismically slipping faults (Bisrat et al., 2014; Dunn et al., 2013). The high-resolution three-dimensional P-wave seismic attenuation structure as well as abnormally low S-wave (V_S) and modestly reduced P-wave

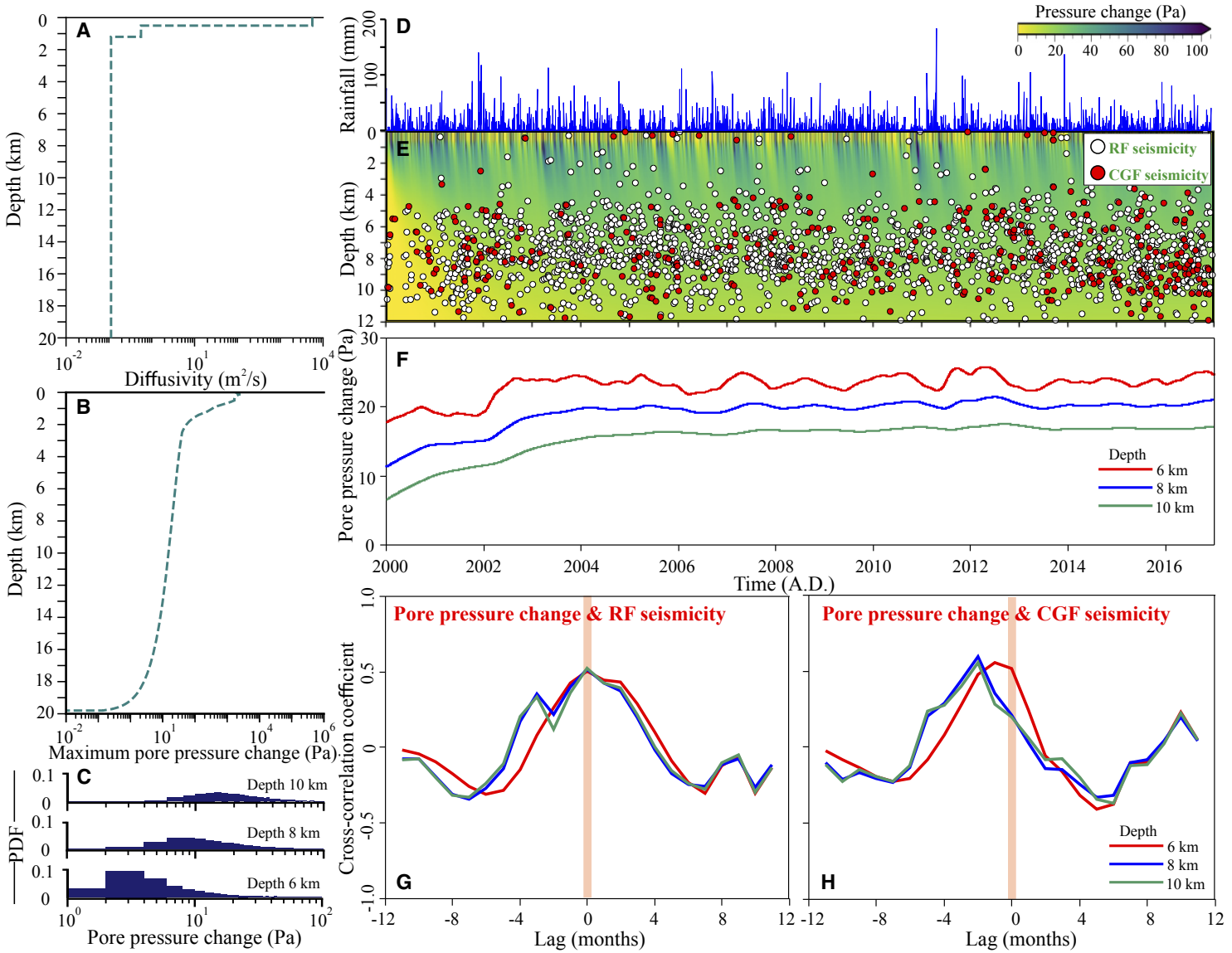

Figure 6. (A, B) Variation of diffusivity and associated pore pressure change as a function of depth below the surface. Model-based varying porosity and permeability parameters with depth layers have been considered (Table S2 [see text footnote 1]). (C) Probability density function (PDF) of modeled pressure change at depths 6 km, 8 km, and 10 km below the surface. (D) Variation in rainfall with time for the period 2000–2017. (E) Pore pressure change obtained from model as function of depth and time by considering daily rainfall from the Tropical Rainfall Measuring Mission over the period 2000–2017. Seismicity associated with Reelfoot fault (RF) and Cottonwood Grove fault (CGF) is represented by white and red circles, respectively. Color scale indicates pressure change. (F) Pore pressure changes with time at depth 6 km, 8 km, and 10 km. (G, H) Cross-correlation coefficient of the pore pressure change at depth of 6 km, 8 km, and 10 km with seismicity associated with Reelfoot and Cottonwood Grove faults, respectively.

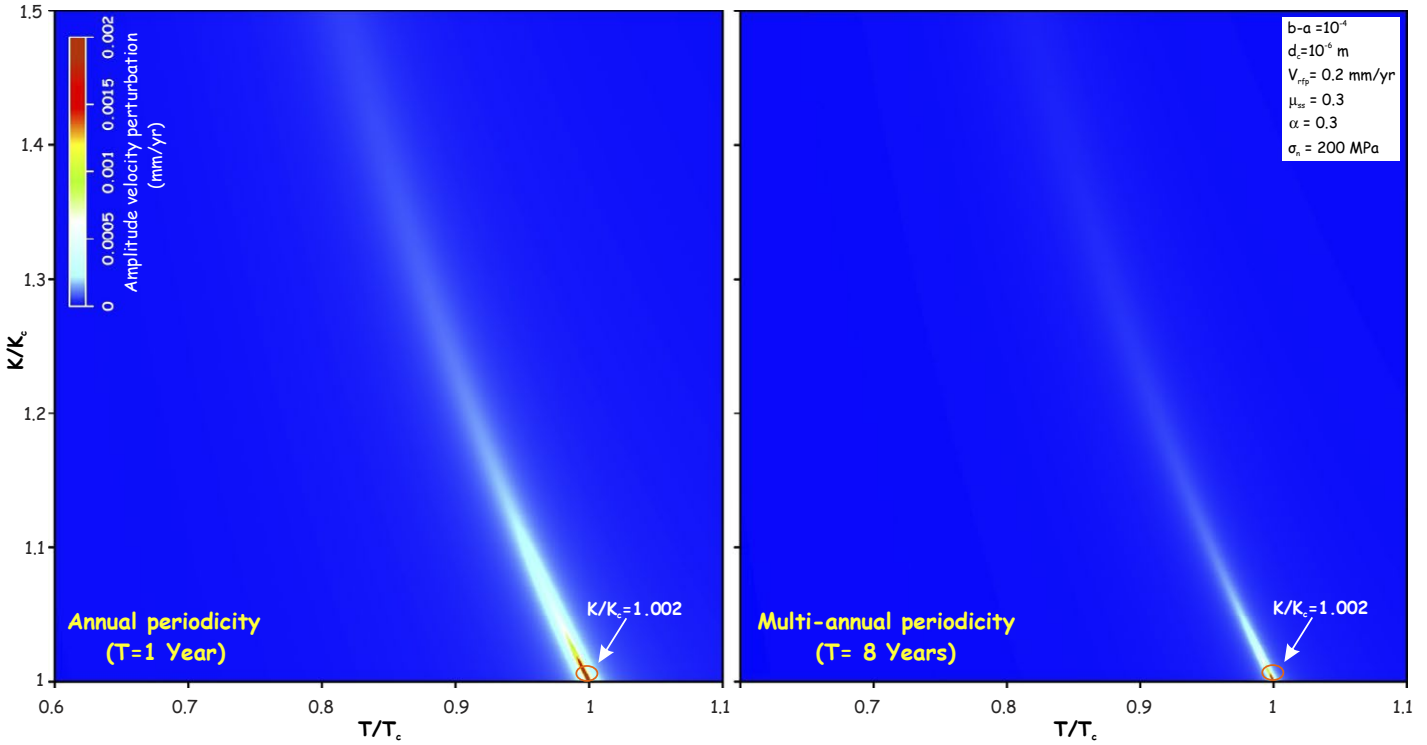

Figure 7. Effect of fault resonance process and role of varying pore fluid pressure, shown as amplitude velocity perturbation as a function of period *T* and fault stiffness for specific frictional parameters. Parameters shown in the inset box: V_{rfm}—fault motion velocity; μ_{ss}—steady state frictional coefficient; d_c—critical slip distance; *b*-*a*—frictional parameters; α—frictional response to change in normal stress; σ_n—effective normal stress. Left and right panels show amplitude velocity perturbation for annual and multi-annual period. Note that amplitude velocity perturbation is maximum when the fault elastic stiffness (*K*) is very close to critical stiffness of fault (K_c) and period of excitation (*T*) is very close to critical time period (T_c).

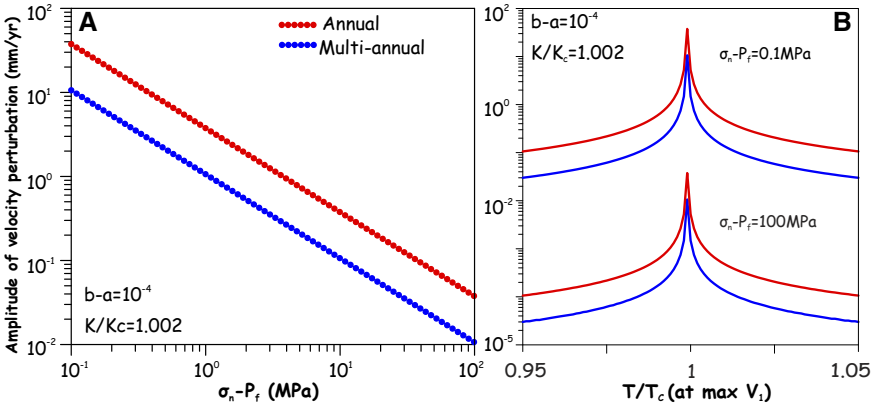

Figure 8. (A) Variation of amplitude velocity perturbation as a function of effective normal stress (pore fluid pressure). (B) For the respective value of effective normal stress, amplitude velocity perturbation approaches maximum for K/K_c = 1.002. V_1—amplitude of slip perturbation; *b*–*a*—frictional parameters; K_c—critical stiffness of fault; *K*—fault elastic stiffness; T_c—critical time period; *T*—period of excitation; P_f—pore fluid pressure. Note a low value of effective normal stress favors a higher-amplitude velocity perturbation (i.e., fault resonance process) and vice versa.

(V_P) velocities (or high V_P/V_S ratio) along the NMSZ provide information about the material properties surrounding the fault zones (Bisrat et al., 2014; Dunn et al., 2013). The domains of reported high swarm activity attributed to fluid-rich fractures along the Reelfoot fault (Bisrat et al., 2014; Dunn et al., 2013) coincide with the zones of highest attenuation (i.e., reduction of Q_P [attenuation factor]) and high V_P/V_S ratio (Fig. S13, see footnote 1). In contrast, such type of fluid activity is lacking in the case of the Cottonwood Grove fault (Fig. S13). Furthermore, it appears that the zone of anomalous fluid-rich fractures along the Reelfoot fault segment coincides with the depth range (~4–10 km depth) of the strongest seismicity modulation on inter-annual and annual time scales (Fig. S14). The presence of anomalous fluid-rich crust in the Reelfoot fault may have a direct impact on the fault frictional rheology and susceptibility to the seismicity modulation process. The presence of anomalously pressurized pore fluids in the Reelfoot fault segment could significantly reduce the value of the critical magnitude of the normal stress perturbation on to the order of 10^{-3} and thus facilitate the resonance destabilization process, which may not be the case for the Cottonwood Grove fault segment (Fig. 9). We suggest that during drought-induced prolonged drier periods and seasonal unloading conditions,

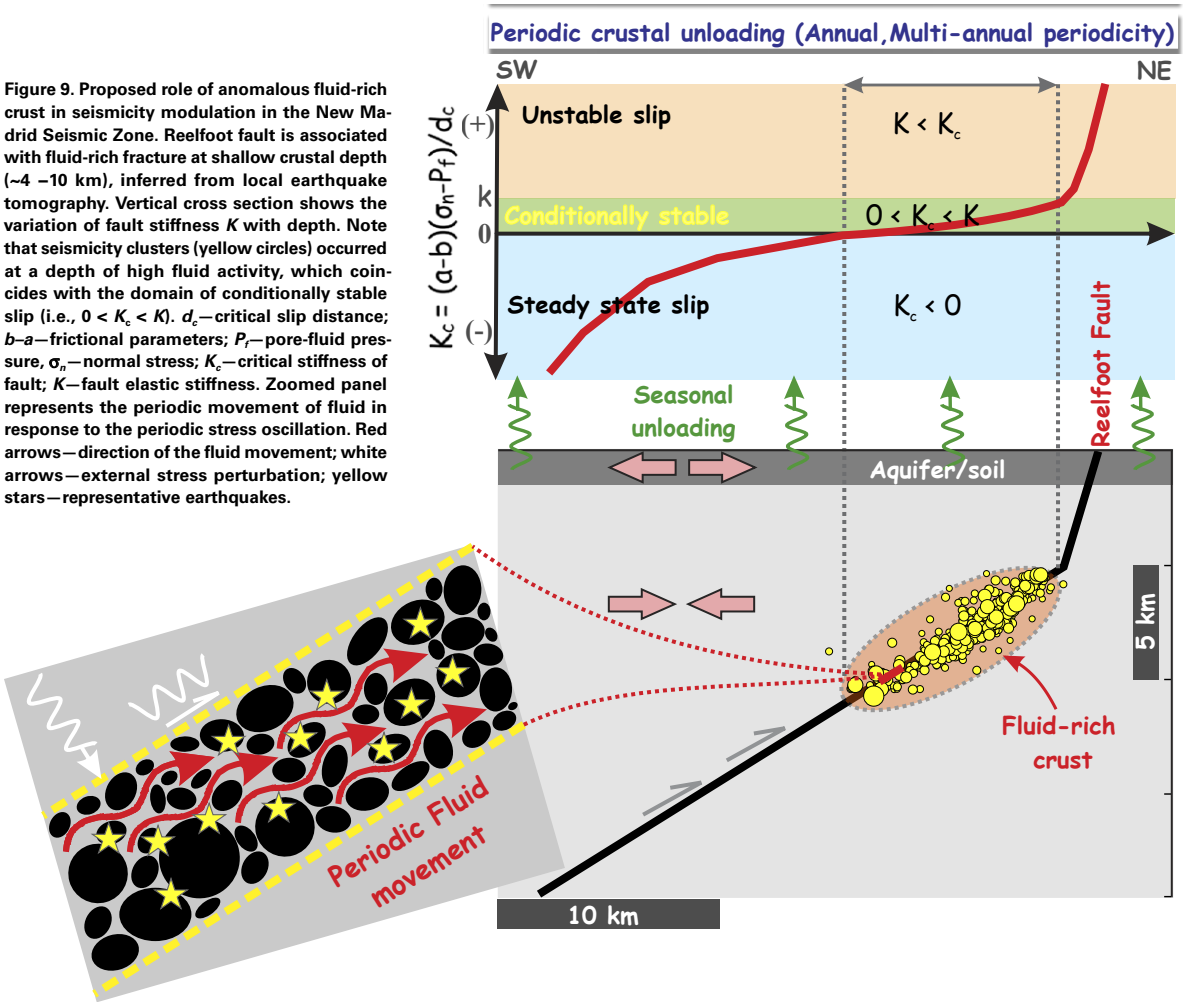

Figure 9. Proposed role of anomalous fluid-rich crust in seismicity modulation in the New Madrid Seismic Zone. Reelfoot fault is associated with fluid-rich fracture at shallow crustal depth (~4 –10 km), inferred from local earthquake tomography. Vertical cross section shows the variation of fault stiffness *K* with depth. Note that seismicity clusters (yellow circles) occurred at a depth of high fluid activity, which coincides with the domain of conditionally stable slip (i.e., $0 < K_c < K$). d_c—critical slip distance; *b–a*—frictional parameters; P_f—pore-fluid pressure, σ_n—normal stress; K_c—critical stiffness of fault; *K*—fault elastic stiffness. Zoomed panel represents the periodic movement of fluid in response to the periodic stress oscillation. Red arrows—direction of the fluid movement; white arrows—external stress perturbation; yellow stars—representative earthquakes.

the shallow soil skeleton and aquifer undergo contraction whereas basement rock undergoes expansion, which is favorable for promoting a thrust fault during unloading conditions, modulating the effective stress regime and the seismicity rate on the Reelfoot fault (Figs. 7 and 8).

We acknowledge that previous studies have also suggested seismicity modulation in the NMSZ at annual periods (Craig et al., 2017; Costain, 2008). Costain (2008) highlighted the spatiotemporal correlation between surface stream flow attributes (mean annual stream flow and standard deviation of stream flow) and the NMSZ seismicity. It has been proposed that fluctuations in the elevation of the water table (river stage) are associated with pore-fluid pressure transients that are transmitted to hypocentral depths and trigger earthquakes through a poroelastic diffusion process (Costain, 2008). On the other hand, Craig et al. (2017) correlated the rate of micro-earthquakes in the NMSZ at annual and multi-annual time scales with periodic hydrological surface loading in the upper Mississippi embayment. Previous study on the rate of earthquakes on both an annual and a multi-annual scale showed that earthquakes are caused by elastic stresses induced by the hydrological load in the NMSZ (Craig et al., 2017). Also, Craig et al. (2017) suggested that the slow secular stressing rate at the NMSZ leads to a critical period of stress variation should $T_c \gtrsim 10$, where $T_c = 2\pi a\sigma(\dot{\tau})^{-1}$, (where a is the rate-and-state fault frictional parameter, σ is the effective normal stress, and $\dot{\tau}$ is the secular stressing rate). Thus, the NMSZ fault system is sensitive to loading at both annual and multi-annual periods. However, this appears to be a general explanation for seismicity modulation, which can be applicable for all stable plate interior regions but not explicitly for specific multi-annual periodicity. Moreover, in the focus of earthquake physics, neither of the earlier studies could demonstrate the specific relation between seismicity modulation in the Reelfoot fault and Cottonwood Grove fault, respectively. It has not been explained why the seismicity modulation on both an annual and a multi-annual scale explicitly is observed in the Reelfoot fault segment and the reason for lack of such modulation in the case of the Cottonwood Grove fault segment. In the present study, we have demonstrated all these caveats and also bring out the specific relationship between seismicity modulation and prolonged drought conditions in the NMSZ region.

The relationship between climatic phenomena and seismicity variation can also be tested on other plate interior regions—such as the Kutch region in Gujarat, India; the Delhi seismic zone in India; Nordland, Northern Norway; the Eastern Tennessee Seismic Zone, USA; and the north China region. Recently, Pfeffer et al. (2023) investigated six to eight years' periodicity in the Earth system and suggested that it is linked with various climatic phenomena, such as global mean sea level, Pacific Decadal Oscillation, North Atlantic Oscillation, Atlantic Multidecadal Oscillation, and ENSO. Further, they suggested that GRACE and GRACE Follow-On Terrestrial Water Storage in the NMSZ region also show prominent multi-annual cycles (Fig. S15). Therefore, in addition to the ENSO event, it is also necessary to investigate the impact of other climatic phenomena on seismicity modulation in plate boundary and plate interior regions. However, the physical connection between these climatic phenomena and seismicity modulation is difficult to establish. Hence, we have not explored these possibilities and factors further in the present study.

CONCLUDING REMARKS

Our present findings clearly reveal a long-term relationship between the variation of hydrological load–induced stress perturbation and seismicity modulation in the stable plate interior region of the NMSZ. The seismicity rate of the Reelfoot fault segment on the multi-annual and seasonal time scale is influenced by the prolonged drought period, which is linked with climatic variability like ENSO events. Moreover, the rate of seismicity in the Reelfoot fault segment increases by ~60% during the drier period relative to the wet period. Also, the fault resonance model demonstrates that near-lithostatic pore pressures lead to an increase in the amplitude of the velocity perturbation, making the Reelfoot fault segment more susceptible for seismicity modulation, which is not the case for the Cottonwood Grove fault segment. Hence, climate variability–induced changes in terrestrial water storage appear to be a potential driver for elevating earthquake hazards in the stable plate interiors.

ACKNOWLEDGMENTS

This work is financially supported by the Chinese National Key Research and Development Program (grant 2021YFA0716100 to Jin) and Ministry of Earth Science India [grant MoES/P.O.(Seismo)/1(235)/2014 to Kundu]. Senapati is supported by a NITR research fellowship. We thank Science Editor Andrea Hampel, Associate Editor Craig H. Jones, three anonymous reviewers, and William Holt for their constructive comments, which improved the quality of the manuscript.

REFERENCES CITED

Ader, T.J., and Avouac, J.-P., 2013, Detecting periodicities and declustering in earthquake catalogs using the Schuster spectrum, application to Himalayan seismicity: Earth and Planetary Science Letters, v. 377, p. 97–105, https://doi.org/10.1016/j.epsl.2013.06.032.

Aki, K., 1965, Maximum likelihood estimate of *b* in the formula log *N* = *a* – *bM* and its confidence limits: Bulletin of the Earthquake Research Institute, University of Tokyo, v. 43, p. 237–239.

Bakun, W.H., and Hopper, M.G., 2004, Magnitudes and locations of the 1811–1812 New Madrid, Missouri, and the 1886 Charleston, South Carolina, earthquakes: Bulletin of the Seismological Society of America, v. 94, p. 64–75, https://doi.org/10.1785/0120020122.

Barton, G., 1989, Elements of Green's Functions and Propagation: Potentials, Diffusion, and Waves (1st edition): Oxford, UK, Oxford University Press, 465 p.

Bettinelli, P., Avouac, J.-P., Flouzat, M., Bollinger, L., Ramillien, G., Rajaure, S., and Sapkota, S., 2008, Seasonal variations of seismicity and geodetic strain in the Himalaya induced by surface hydrology: Earth and Planetary Science Letters, v. 266, p. 332–344, https://doi.org/10.1016/j.epsl.2007.11.021.

Biot, M.A., 1962, Mechanics of deformation and acoustic propagation in porous media: Journal of Applied Physics, v. 33, p. 1482–1498, https://doi.org/10.1063/1.1728759.

Bisrat, S.T., DeShon, H.R., and Rowe, C.A., 2012, Microseismic swarm activity in the New Madrid Seismic Zone: Bulletin of the Seismological Society of America, v. 102, p. 1167–1178, https://doi.org/10.1785/0120100315.

Bisrat, S.T., DeShon, H.R., Pesicek, J., and Thurber, C., 2014, High-resolution 3-D *P* wave attenuation structure of the New Madrid Seismic Zone using local earthquake tomography: Journal of Geophysical Research: Solid Earth, v. 119, p. 409–424, https://doi.org/10.1002/2013JB010555.

Bollinger, L., Perrier, F., Avouac, J.-P., Sapkota, S., Gautam, U., and Tiwari, D.R., 2007, Seasonal modulation of seismicity in the Himalaya of Nepal: Geophysical Research Letters, v. 34, L08304, https://doi.org/10.1029/2006GL029192.

Boussinesq, J., 1885, Application des potentiels à l'étude de l'équilibre et du mouvement des solides élastiques (reprint, 1969): Paris, A. Blanchard, 723 p.

Boyd, O.S., and Cramer, C.H., 2014, Estimating earthquake magnitudes from reported intensities in the central and eastern United States: Bulletin of the Seismological Society of America, v. 104, p. 1709–1722, https://doi.org/10.1785/0120120352.

Broomhead, D.S., and King, G.P., 1986, On the qualitative analysis of experimental dynamical systems, *in* Sarkar, S., ed., Nonlinear Phenomena and Chaos: Bristol, UK, Adam Hilger, p. 113–144.

Calais, E., and Stein, S., 2009, Time-variable deformation in the New Madrid Seismic Zone: Science, v. 323, p. 1442, https://doi.org/10.1126/science.1168122.

Calais, E., Freed, A.M., Van Arsdale, R., and Stein, S., 2010, Triggering of New Madrid seismicity by late-Pleistocene erosion: Nature, v. 466, p. 608–611, https://doi.org/10.1038/nature09258.

Calais, E., Camelbeeck, T., Stein, S., Liu, M., and Craig, T.J., 2016, A new paradigm for large earthquakes in stable continental plate interiors: Geophysical Research Letters, v. 43, p. 10,621–10,637, https://doi.org/10.1002/2016GL070815.

Camelbeeck, T., Vanneste, K., Alexandre, P., Verbeeck, K., Petermans, T., Rosset, P., Everaerts, M., Warnant, R., and Van Camp, M., 2007, Relevance of active faulting and seismicity studies to assessment of long-term earthquake activity and maximum magnitude in intraplate northwest Europe, between the Lower Rhine Embayment and the North Sea, *in* Stein, S., and Mazzotti, S., eds., Continental Intraplate Earthquakes: Science, Hazard, and Policy Issues: Geological Society of America Special Paper 425, p. 193–224, https://doi.org/10.1130/2007.2425(14).

Cardozo, N., and Allmendinger, R.W., 2009, SSPX: A program to compute strain from displacement/velocity data: Computers & Geosciences, v. 35, p. 1343–1357, https://doi.org/10.1016/j.cageo.2008.05.008.

Chanard, K., Avouac, J.P., Ramillien, G., and Genrich, J., 2014, Modeling deformation induced by seasonal variations of continental water in the Himalaya region: Sensitivity to Earth elastic structure: Journal of Geophysical Research: Solid Earth, v. 119, p. 5097–5113, https://doi.org/10.1002/2013JB010451.

Constantin, P., Foias, C., Nicolaenko, B., and Temam, R., 1989, Integral Manifolds and Inertial Manifolds for Dissipative Partial Differential Equations: New York, Springer-Verlag, 122 p., https://doi.org/10.1007/978-1-4612-3506-4.

Costain, J.K., 2008, Intraplate seismicity, hydroseismicity, and predictions in hindsight: Seismological Research Letters, v. 79, p. 578–589, https://doi.org/10.1785/gssrl.79.4.578.

Craig, T.J., and Calais, E., 2014, Strain accumulation in the New Madrid and Wabash Valley seismic zones from 14 years of continuous GPS observation: Journal of Geophysical Research: Solid Earth, v. 119, p. 9110–9129, https://doi.org/10.1002/2014JB011498.

Craig, T.J., Chanard, K., and Calais, E., 2017, Hydrologically-driven crustal stresses and seismicity in the New Madrid Seismic Zone: Nature Communications, v. 8, 2143, https://doi.org/10.1038/s41467-017-01696-w.

Craig, T.J., Calais, E., Fleitout, L., Bollinger, L., and Scotti, O., 2023, Time-variable strain and stress rates induced by Holocene glacial isostatic adjustment in continental interiors: Tectonophysics, v. 854, https://doi.org/10.1016/j.tecto.2023.229815.

Deng, K., Zhou, S., Wang, R., Robinson, R., Zhao, C., and Cheng, W., 2010, Evidence that the 2008 M_w 7.9 Wenchuan earthquake could not have been induced by the Zipingpu reservoir: Bulletin of the Seismological Society of America, v. 100, p. 2805–2814, https://doi.org/10.1785/0120090222.

Dunn, M., DeShon, H.R., and Powell, C.A., 2013, Imaging the New Madrid Seismic Zone using double-difference tomography: Journal of Geophysical Research: Solid Earth, v. 118, p. 5404–5416, https://doi.org/10.1002/jgrb.50384.

Ervin, C.P., and McGinnis, L.D., 1975, Reelfoot rift: Reactivated precursor to the Mississippi embayment: Geological Society of America Bulletin, v. 86, p. 1287–1295, https://doi.org/10.1130/0016-7606(1975)86<1287:RRRPTT>2.0.CO;2.

Farquharson, J.I., and Amelung, F., 2020, Extreme rainfall triggered the 2018 rift eruption at Kīlauea Volcano: Nature, v. 580, p. 491–495, https://doi.org/10.1038/s41586-020-2172-5.

Fu, Y., Freymueller, J.T., and Jensen, T., 2012, Seasonal hydrological loading in southern Alaska observed by GPS and GRACE: Geophysical Research Letters, v. 39, L15310, https://doi.org/10.1029/2012GL052453.

Gershunov, A., and Barnett, T.P., 1998, Interdecadal modulation of ENSO teleconnections: Bulletin of the American Meteorological Society, v. 79, p. 2715–2725, https://doi.org/10.1175/1520-0477(1998)079<2715:IMOET>2.0.CO;2.

Ghil, M., Allen, M.R., Dettinger, M.D., Ide, K., Kondrashov, D., Mann, M.E., Robertson, A.W., Saunders, A., Tian, Y., Varadi, F., and Yiou, P., 2002, Advanced spectral methods for climatic time series: Reviews of Geophysics, v. 40, 1003, https://doi.org/10.1029/2000RG000092.

Gold, R.D., DuRoss, C.B., Delano, J.E., Jibson, R.W., Briggs, R.W., Mahan, S.A., Williams, R.A., and Corbett, D.R., 2019, Four major Holocene earthquakes on the Reelfoot fault recorded by sackungen in the New Madrid seismic zone, USA: Journal of Geophysical Research: Solid Earth, v. 124, p. 3105–3126, https://doi.org/10.1029/2018JB016806.

Gomberg, J., 2010, Lessons from (triggered) tremor: Journal of Geophysical Research: Solid Earth, v. 115, B10302, https://doi.org/10.1029/2009JB007011.

Groth, A., and Ghil, M., 2015, Monte Carlo singular spectrum analysis (SSA) revisited: Detecting oscillator clusters in multivariate datasets: Journal of Climate, v. 28, p. 7873–7893, https://doi.org/10.1175/JCLI-D-15-0100.1.

Hainzl, S., Kraft, T., Wassermann, J., Igel, H., and Schmedes, E., 2006, Evidence for rainfall-triggered earthquake activity: Geophysical Research Letters, v. 33, L19303, https://doi.org/10.1029/2006GL027642.

Hough, S.E., and Page, M., 2011, Towards a consistent model for strain accrual and release for the New Madrid Seismic Zone, central United States: Journal of Geophysical Research: Solid Earth, v. 116, B03311, https://doi.org/10.1029/2010JB007783.

Jaeger, J.C., and Cook, N.G.W., 1979, Fundamentals of Rock Mechanics (3rd edition): London, Chapman and Hall, 593 p.

Jaeger, J.C., Cook, N.G.W., and Zimmerman, R.W., 2007, Fundamentals of Rock Mechanics (4th edition): Malden, Massachusetts, Blackwell Publishing, 475 p.

Johnson, C.W., Fu, Y., and Bürgmann, R., 2017, Seasonal water storage, stress modulation, and California seismicity: Science, v. 356, p. 1161–1164, https://doi.org/10.1126/science.aak9547.

Kim, J., Holt, W.E., Bahadori, A., and Shen, W., 2021, Repeating nontectonic seasonal stress changes and a possible triggering mechanism of the 2019 Ridgecrest earthquake sequence in California: Journal of Geophysical Research: Solid Earth, v. 126, https://doi.org/10.1029/2021JB022188.

King, G.C.P., Stein, R.S., and Lin, J., 1994, Static stress changes and the triggering of earthquakes: Bulletin of the Seismological Society of America, v. 84, no. 3, p. 935–953.

Kraner, M.L., Holt, W.E., and Borsa, A.A., 2018, Seasonal nontectonic loading inferred from cGPS as a potential trigger for the M6.0 South Napa earthquake: Journal of Geophysical Research: Solid Earth, v. 123, p. 5300–5322, https://doi.org/10.1029/2017JB015420.

Kundu, B., Vissa, N.K., and Gahalaut, V.K., 2015, Influence of anthropogenic groundwater unloading in Indo-Gangetic plains on the 25 April 2015 Mw 7.8 Gorkha, Nepal earthquake: Geophysical Research Letters, v. 42, p. 10,607–10,613, https://doi.org/10.1002/2015GL066616.

Kundu, B., Vissa, N.K., Panda, D., Jha, B., Asaithambi, R., Tyagi, B., and Mukherjee, S., 2017, Influence of a meteorological cycle in mid-crustal seismicity of the Nepal Himalaya: Journal of Asian Earth Sciences, v. 146, p. 317–325, https://doi.org/10.1016/j.jseaes.2017.06.003.

Lowry, A.R., 2006, Resonant slow fault slip in subduction zones forced by climatic load stress: Nature, v. 442, p. 802–805, https://doi.org/10.1038/nature05055.

McKenna, J., Stein, S., and Stein, C.A., 2007, Is the New Madrid seismic zone hotter and weaker than its surroundings?, *in* Stein, S., and Mazzotti, S., ed., Continental Intraplate Earthquakes: Science, Hazard, and Policy Issues: Geological Society of America Special Paper 425, p. 167, https://doi.org/10.1130/2007.2425(12).

Menke, W., 1984, Geophysical Data Analysis: Discrete Inverse Theory: Orlando, Florida, Academic Press, 260 p., https://doi.org/10.1016/B978-0-12-490920-5.X5001-7.

Munoz, S.E., and Dee, S.G., 2017, El Niño increases the risk of lower Mississippi River flooding: Scientific Reports, v. 7, 1772, https://doi.org/10.1038/s41598-017-01919-6.

Panda, D., Kundu, B., Gahalaut, V.K., Bürgmann, R., Jha, B., Asaithambi, R., Yadav, R.K., Vissa, N.K., and Bansal, A.K., 2018, Seasonal modulation of deep slow-slip and earthquakes on the Main Himalayan Thrust: Nature Communications, v. 9, 4140, https://doi.org/10.1038/s41467-018-06371-2.

Peng, Z., Vidale, J.E., Wech, A.G., Nadeau, R.M., and Creager, K.C., 2009, Remote triggering of tremor along the San Andreas Fault in central California: Journal of Geophysical Research: Solid Earth, v. 114, B00A06, https://doi.org/10.1029/2008JB006049.

Perfettini, H., and Schmittbuhl, J., 2001, Periodic loading on a creeping fault: Implications for tides: Geophysical Research Letters, v. 28, p. 435–438, https://doi.org/10.1029/2000GL011686.

Perfettini, H., Schmittbuhl, J., Rice, J.R., and Cocco, M., 2001, Frictional response induced by time-dependent fluctuations of the normal loading: Journal of Geophysical Research: Solid Earth, v. 106, p. 13,455–13,472, https://doi.org/10.1029/2000JB900366.

Pfeffer, J., Cazenave, A., Rosat, S., Moreira, L., Mandea, M., Dehant, V., and Coupry, B., 2023, A 6-year cycle in the Earth system: Global and Planetary Change, v. 229, https://doi.org/10.1016/j.gloplacha.2023.104245.

Plaut, G., and Vautard, R., 1994, Spells of low-frequency oscillations and weather regimes in the Northern Hemisphere: Journal of the Atmospheric Sciences, v. 51, p. 210–236, https://doi.org/10.1175/1520-0469(1994)051<0210:SOLFOA>2.0.CO;2.

Pollitz, F.F., Wech, A., Kao, H., and Bürgmann, R., 2013, Annual modulation of non-volcanic tremor in northern Cascadia: Journal of Geophysical Research: Solid Earth, v. 118, p. 2445-2459. https://doi.org/10.1002/jgrb.50181.

Roeloffs, E.A., 1988, Fault stability changes induced beneath a reservoir with cyclic variations in water level: Journal of Geophysical Research: Solid Earth, v. 93, p. 2107–2124, https://doi.org/10.1029/JB093iB03p02107.

Rudnicki, J.W., 1986, Fluid mass sources and point forces in linear elastic diffusive solids: Mechanics of Materials, v. 5, p. 383–393, https://doi.org/10.1016/0167-6636(86)90042-6.

Senapati, B., Kundu, B., and Jin, S., 2022, Seismicity modulation by external stress perturbations in plate boundary vs. stable plate interior: Geoscience Frontiers, v. 13, https://doi.org/10.1016/j.gsf.2022.101352.

Senapati, B., Kundu, B., Perfettini, H., Gahalaut, V.K., Singh, A.K., Ghosh, A., and Rao, N.P., 2023, Fault resonance process and its implications on seismicity modulation on the active fault system: Tectonophysics, v. 861, https://doi.org/10.1016/j.tecto.2023.229920.

Shen, Z.K., Jackson, D.D., and Ge, B.X., 1996, Crustal deformation across and beyond the Los Angeles basin from geodetic measurements: Journal of Geophysical Research: Solid Earth, v. 101, p. 27,957–27,980, https://doi.org/10.1029/96JB02544.

Smith, S.R., Green, P.M., Leonardi, A.P., and O'Brien, J.J., 1998, Role of multiple-level tropospheric circulations in forcing ENSO winter precipitation anomalies: Monthly Weather Review, v. 126, p. 3102–3116, https://doi.org/10.1175/1520-0493(1998)126<3102:ROMLTC>2.0.CO;2.

Stein, R.S., 1999, The role of stress transfer in earthquake occurrence: Nature, v. 402, p. 605–609, https://doi.org/10.1038/45144.

Stein, S., and Liu, M., 2009, Long aftershock sequences within continents and implications for earthquake hazard assessment: Nature, v. 462, p. 87–89, https://doi.org/10.1038/nature08502.

Temam, R., 1997, Infinite-Dimensional Dynamical Systems in Mechanics and Physics (2nd edition): New York, Springer-Verlag, 648 p., https://doi.org/10.1007/978-1-4612-0645-3.

Thomas, A.M., Nadeau, R.M., and Bürgmann, R., 2009, Tremor-tide correlations and near-lithostatic pore pressure on the deep San Andreas fault: Nature, v. 462, p. 1048–1051, https://doi.org/10.1038/nature08654.

Turcotte, D.L., and Schubert, G., 2002, Geodynamics (2nd edition): Cambridge, UK, Cambridge University Press, 456 p., https://doi.org/10.1017/CBO9780511807442.

Tuttle, M.P., Schweig, E.S., III, Campbell, J., Thomas, P.M., Sims, J.D., and Lafferty, R.H.,III, 2005, Evidence for New Madrid earthquakes in A.D. 300 and 2340 B.C.: Seismological Research Letters, v. 76, p. 489–501, https://doi.org/10.1785/gssrl.76.4.489.

Williams, R.A., 2009, Earthquake Hazard in the New Madrid Seismic Zone Remains a Concern: U.S. Geological Survey Fact Sheet 2009–3071, https://pubs.usgs.gov/fs/2009/3071/pdf/FS09-3071.pdf.

Young, Z.M., Kreemer, C., and Blewitt, G., 2021, GPS constraints on drought-induced groundwater loss around Great Salt Lake, Utah, with implications for seismicity modulation: Journal of Geophysical Research: Solid Earth, v. 126, https://doi.org/10.1029/2021JB022020.

Zaliapin, I., and Ben-Zion, Y., 2020, Earthquake declustering using the nearest-neighbor approach in space-time-magnitude domain: Journal of Geophysical Research: Solid Earth, v. 125, https://doi.org/10.1029/2018JB017120.

Ziv, A., and Rubin, A.M., 2000, Static stress transfer and earthquake triggering: No lower threshold in sight?: Journal of Geophysical Research: Solid Earth, v. 105, p. 13,631–13,642, https://doi.org/10.1029/2000JB900081.